Advances in
Geo-Energy Research
Vol. 18, No. 1, p. 38-50, 2025

Original article

Machine learning potential insights into mechanical response and heat transfer in CO_2 hydrate

Kaibin Xiong[1], Yuan Li[2], Ziyan Lin[2], Gaoyang Luo[2], Jianyang Wu[2,3]*

[1]*College of Life Sciences, Wuchang University of Technology, Wuhan 430223, P. R. China*

[2]*Research Institute for Biomimetics and Soft Matter, Jiujiang Research Institute and Fujian Provincial Key Laboratory for Soft Functional Materials Research, Xiamen University, Xiamen 361005, P. R. China*

[3]*NTNU Nanomechanical Lab, Norwegian University of Science and Technology, Trondheim 7491, Norway*

Keywords:
CO_2 hydrate
mechanical properties
thermal conductivity
deep potential
molecular dynamics

Cited as:
Xiong, K., Li, Y., Lin, Z., Luo, G., Wu, J. Machine learning potential insights into mechanical response and heat transfer in CO_2 hydrate. Advances in Geo-Energy Research, 2025, 18(1): 38-50.
https://doi.org/10.46690/ager.2025.10.04

Abstract:
Accurate prediction of the mechanical and thermal properties of CO_2 hydrates is essential for their applications in carbon sequestration and refrigeration, yet remains challenging with empirical forcefields. In this work, a deep potential machine learning potential for CO_2 hydrate, trained on density functional theory datasets, is for the first time developed to serve as a unified and accurate computational framework. The as-developed deep potential machine learning potential achieves near-density functional theory accuracy in energy, force, and virial stress predictions while enabling large-scale molecular dynamics simulations at significantly reduced computational cost. Uniaxial stress-strain analyses demonstrate that the model captures the tensile strength and progressive ductile-like failure behavior. Thermal conductivity prediction agrees closely with experimental measurements within 2% deviation, outperforming empirical forcefields. Vibrational dynamics and phonon analyses reveal that the deep potential machine learning potential more accurately describes the anharmonicity and phonon scattering, especially in high-frequency modes, yielding physically realistic thermal transport behavior. This work establishes deep potential machine learning potential as a robust tool for advancing CO_2 hydrate-based technologies by providing a path for accurate and efficient multi-property prediction.

1. Introduction

CO_2 hydrates are crystalline inclusion compounds in which guest CO_2 molecules are encapsulated within hydrogen (H)-bonded water cages under specific low-temperature and high-pressure conditions (Warrier et al., 2018). Compared with methane hydrates (Lin et al., 2022), CO_2 hydrates exhibit superior thermodynamic stability below 283 K and require lower equilibrium pressures for formation (Kang et al., 2001; Chen et al., 2009). These characteristics make them promising materials for a variety of applications, including natural gas exploration, carbon capture and storage (CCS) and refrigeration technologies (Zhang et al., 2024b, 2024c; Hassanpouryouzband et al., 2020; Yin et al., 2021; Lu et al., 2023).

Despite these prospects, the practical deployment of CO_2 hydrate-based technologies requires a comprehensive understanding of their physical properties, yet substantial knowledge gaps remain. In particular, characterization of their mechanical behavior is crucial for ensuring geological stability during CO_2 sequestration. However, experimental data for monocrystalline CO_2 hydrates are still lacking, and computational investigations remain limited. Previous molecular dynamics (MD) simulations have shown inconsistencies arising from forcefield selection (Jia et al., 2017; Shi et al., 2018; Xu et al., 2020; Zhang et al., 2023; Zhang et al., 2024b, 2024c). For instance, Liu et al. (2022) reported Young's moduli of 5.17-6.18 GPa

---

Yandy Scientific Press

*Corresponding author.
E-mail address: kbxiong@wut.edu.cn (K. Xiong); 19820231153961@stu.xmu.edu.cn (Y. Li); 9820221153861@stu.xmu.edu.cn (Z. Lin); 19820250157780@stu.xmu.edu.cn (G. Luo); jianyang@xmu.edu.cn (J. Wu).

Received July 29, 2025; revised August 24, 2025; accepted September 15, 2025; available online September 18, 2025.

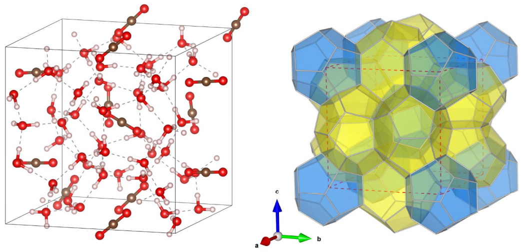

Fig. 1. Structure diagram of sI CO_2 hydrate. (Left) Molecular configuration of the unit-cell. (Right) Clathrate cage configuration, where blue and yellow indicate 5^{12} and $5^{12}6^2$ cages, respectively.

and tensile strengths of 0.454-0.745 GPa. In contrast, Shi et al. (2018) calculated Young's moduli of 5.07-6.50 GPa and tensile strengths of 0.192-0.789 GPa. Such discrepancies, largely attributable to differences in water forcefields, restrict the predictive reliability of conventional MD simulations.

Accurate evaluation of thermal conductivity is equally crucial, as it governs heat transfer in hydrate-bearing sediments and refrigeration systems, thereby influencing phase transformation kinetics and structural stability (Zhang et al., 2024a). However, experimental measurements of CO_2 hydrate thermal conductivity have yielded inconsistent results. Liu et al. (2017) reported values of 0.5530-0.5861 W/(m·K) using the transient plane source method, while Wan et al. (2016) measured values of 0.6394-1.070 W/(m·K) with the same technique. Jiao et al. (2021), employing the 3ω method, measured a lower value of 0.5300 W/(m·K). Similarly, MD simulations exhibit substantial variations depending on the employed water and CO_2 models. Jiang and Jordan et al. (2010) reported approximately 0.8055 W/(m·K) using SPC/E water and the Zhang-Duan CO_2 models (Berendsen et al., 1987; Zhang and Duan et al., 2005), whereas Li et al. (2025) obtained 0.8850 W/(m·K) at 270 K with the OPLS-AA CO_2 model and the TIP4P/Ice water (Jorgensen et al., 1996; Abascal et al., 2005). In contrast, Liu et al. (2021) computed lower values of 0.4836-0.7494 W/(m·K) using the CVFF forcefield (Hagler et al., 1979). Other simulations combing TIP4P water with EPM2 (Jorgensen et al., 1983; Harris and Yung et al., 1995), TraPPE or Zhang-Duan CO_2 models yielded significantly higher values of 1.030-1.157 W/(m·K) (Potoff and Siepmann et al., 2001; Zhang and Duan et al., 2005; Wan et al., 2014). These large variations, primarily due to forcefield dependence, impede reliable thermal transport predictions and pose a critical challenge for applications requiring precise thermal management, such as refrigeration and energy system optimization.

Accurate and simultaneous prediction of mechanical and thermal transport properties is therefore paramount for advancing hydrate-based technologies. Achieving this computationally remains challenging. Although first-principles MD offers high accuracy, it is prohibitively expensive for the large-scale and long-time simulations required for reliable property evaluation. These limitations underscore the promise of machine learning potentials (MLPs), which can attain near-quantum accuracy at computational costs comparable to classical MD. While MLPs have demonstrated considerable success in modelling water-based systems (Luo et al., 2023; Xu et al., 2023; Song et al., 2025), no MLP has yet been developed that can simultaneously and accurately capture both mechanical and thermal transport properties of CO_2 hydrates. This capability is crucial, as these properties are governed by intertwined atomic-scale phenomena, such as anharmonic lattice vibrations and phonon scattering, which are beyond the accurate representation of fixed-formed empirical potentials and remain insufficiently addressed in existing MLP studies. This limitation constrains reliable assessments of hydrate-based CCS and refrigeration technologies, where precise understanding of mechanical stability and thermal efficiency is vital.

To address this specific challenge, a Deep Potential (DP)-based MLP (DP-MLP) for CO_2 hydrate is developed to uniquely bridge this gap. The novelty of this work is threefold. First, unlike empirical potentials, the density functional theory (DFT)-trained DP-MLP inherently capture the anharmonicity and complex phonon scattering, both essential for realistic thermal conductivity prediction. Second, it goes beyond prior MLP studies by demonstrating high fidelity not only in structural and thermal transport properties but also in mechanical responses, including the tensile strength and the progressive failure behavior under tension. Third, it establishes a unified and efficient computational framework that enables, for the first time using an MLP, coupled analysis of thermo-mechanical properties of CO_2 hydrates with near-DFT accuracy. The DP-MLP model is rigorously trained and validated against DFT datasets while maintaining the computational efficiency of classic MD simulations. Systematic benchmarking against empirical water forcefields and DFT confirms its unique capability to accurately reproduce both the coupled mechanical and thermal transport characteristics of CO_2 hydrate. This framework provides a robust and transformative tool for advancing the fundamental understanding and practical applications of hydrate-based CCS and refrigeration technologies.

2. Models and methodology

2.1 Molecular model of CO_2 hydrate

CO_2 hydrate generally crystallizes in the structure I (sI) clathrate form, with $pm\bar{3}n$ space group and a lattice parameter of a = 11.9 Å (Takeuchi et al., 2013). Its unit cell contains 46 water molecules forming two small cages (12 pentagonal faces) and six large cages (12 pentagonal and 2 hexagonal faces), corresponding to an ideal stoichiometry of $8CO_2 \cdot 46H_2O$ under full guest occupancy. The initial atomic positions of the water framework are obtained from X-ray diffraction data, and CO_2 molecules are placed inside the cages as guest species. The molecular and cage configurations of the unit-cell of sI CO_2 hydrate are illustrated in Fig. 1. The model represents an idealized crystal structure with full guest occupancy and no defects, enabling investigation of the intrinsic mechanical and thermal properties of the CO_2 hydrate as a fundamental benchmark. It is noted that real-world systems involve additional complexities such as formation kinetics, polycrystallinity, and structural defects, which are beyond the scope of this study but represent important directions for future research (Xia et al., 2025).

2.2 First-principles calculations and dataset construction

A representative dataset for training a DP-MLP for CO_2 hydrate is generated using first-principles calculations within the framework of DFT, implemented in the Vienna Ab-initio Simulation Package (Kresse and Furthmüller et al., 1996; Hafner et al., 2008). The Kohn-Sham equations are solved using the projector-augmented wave method with standard pseudopotentials for O, H and C atoms. Exchange-correlation interactions are treated with the Perdew-Burke-Ernzerhof functional under the generalized gradient approximation, and van der Waals interactions are included via Grimme's DFT-D3 correction with zero damping. A plane-wave energy cutoff of 750 eV and a Γ-centered 3×3×3 k-point mesh are adopted. The self-consistent field convergence threshold is set to 10^{-5} eV for total energy. Ionic relaxations are performed using the conjugate gradient algorithm until the energy change between successive steps is less than 10^{-5} eV, ensuring fully optimized atomic configurations.

To enhance structural diversity, both 1×1×1 unit-cell and 1×1×2 supercells of sI CO_2 hydrate are constructed. Initial configurations of sI CO_2 hydrate are first subjected to variable-cell optimization to obtain fully relaxed baseline structures. Uniaxial strain is subsequently imposed to these optimized systems, with lattice vectors constrained in all directions, and the resulting configurations are structurally re-optimized to generate tensile deformation data. A strain range of 0-25% is examined, with configurations sampled at 1% strain intervals. Because structural failure typically occurs between 18% and 22% strain, this region is sampled more finely at 0.1% intervals. All strained structures are thermally equilibrated at 270 K for 0.5 ps, and parallel trajectories are generated to improve conformational sampling. Additional heating MD simulations are conducted in the NVT ensemble using a Nosé-Hoover thermostat. For the unit cell model, heating from 250 to 270 K and from 250 to 300 K is performed at a heating rate of 10 K/ps, while the supercell model is heated from 250 to 320 K under identical conditions. All DFT data are rigorously processed and divided into training and test subsets to ensure DFT-level fidelity. The resulting multi-conditional dataset serves as the foundation for the subsequent DP-MLP training and validation.

2.3 Implementation of the DP-MLP potential

The DP-MLP is implemented using the Smooth Edition of the Embedded Atom Descriptor (SE-A) as provided in DeePMD-kit (Wang et al., 2018; Zhang et al., 2020). A cutoff radius of 6 Å and a smoothing cutoff parameter of 0.5 Å are employed to comprehensively capture the atomic local environments. The embedding network consists of three-layers with 20, 50 and 100 neurons, respectively, to encode atomic structural features. ResNet connections are incorporated to enhance the representational capability of the descriptor (Targ et al., 2016). The fitting network is designed as three-layer fully connected neural network with 240 neurons per layer, with the ReLU activation function to improve non-linear modelling capability. The training is performed using an exponential decay learning rate schedule, starting from an initial value of 0.001 and decaying every 5,000 steps. The loss function includes both energy and atomic force components, with initial weighting factors of 0.02 for energy and 1,000 for forces. These weighting factors are dynamically adjusted during training until they reach a value of 1 for both components. The DP-MLP is trained for 300,000 batches to ensure convergence and numerical stability (Arora et al., 2016).

2.4 MD simulations

To characterize the mechanical properties, classic MD simulations are performed on single-crystal CO_2 hydrate with a 3×3×3 supercell configuration. Periodic boundary conditions are applied along the x, y, and z directions to maintain system continuity. Prior to MD simulations, the initial hydrate configuration is geometrically optimized. Subsequently, MD simulations with 200,000 timesteps are performed under the isothermal-isobaric (NPT) ensemble at 270 K and 1 bar. Finally, uniaxial tensile deformation is applied along the z-direction using a strain-controlled approach within NPT ensemble. A strain rate of 108/s is set, which is typical for MD simulations to observe deformation and failure within accessible timescales. The Poisson effect is considered to account for lateral deformation accompanying the tensile loading. For thermal conductivity evaluation, non-equilibrium MD (NEMD) simulations employing the EHEX algorithm are performed on a periodic CO_2 hydrate structure composed of 2×2×10 unit-cells. The system is first equilibrated for 200,000 timesteps under the NPT ensemble at 270 K and 1 bar, followed by an additional 200,000 timesteps under microcanonical ensemble. The NEMD method establishes a heat flux by imposing a temperature gradient across the system, driving it into a non-equilibrium steady state. A constant temperature gradient is maintained by introducing designated heat source and heat sink regions, allowing measurement of the resulting heat flux. The thermal conductivity k is determined from the relation:

$$k = \frac{J_q}{\nabla T} \tag{1}$$

where J_q denotes the heat flux per unit cross-sectional area, and ∇T represents the applied temperature gradient. A timestep of 0.5 fs is used throughout all simulations to ensure numerical stability and computational accuracy.

For comparative analysis, the DP-MLP potential is benchmarked against four empirical water models including TIP4P (Jorgensen et al., 1983), TIP4P/Ice (Abascal et al., 2005), TIP4P/2005 (Abascal and Vega et al., 2005), and TIP4P/Ewald (Horn et al., 2004). The TraPPE forcefield is employed for the CO_2 guest molecules (Potoff and Siepmann et al., 2001). Van der Waals interactions are described using the standard 12-6 Leonard Jones potential, while the long-range Coulombic interactions are computed using the particle-particle-particle method. All classic MD simulations are performed using large scale atomic/molecular massively parallel simulators (Plimpton et al., 1995).

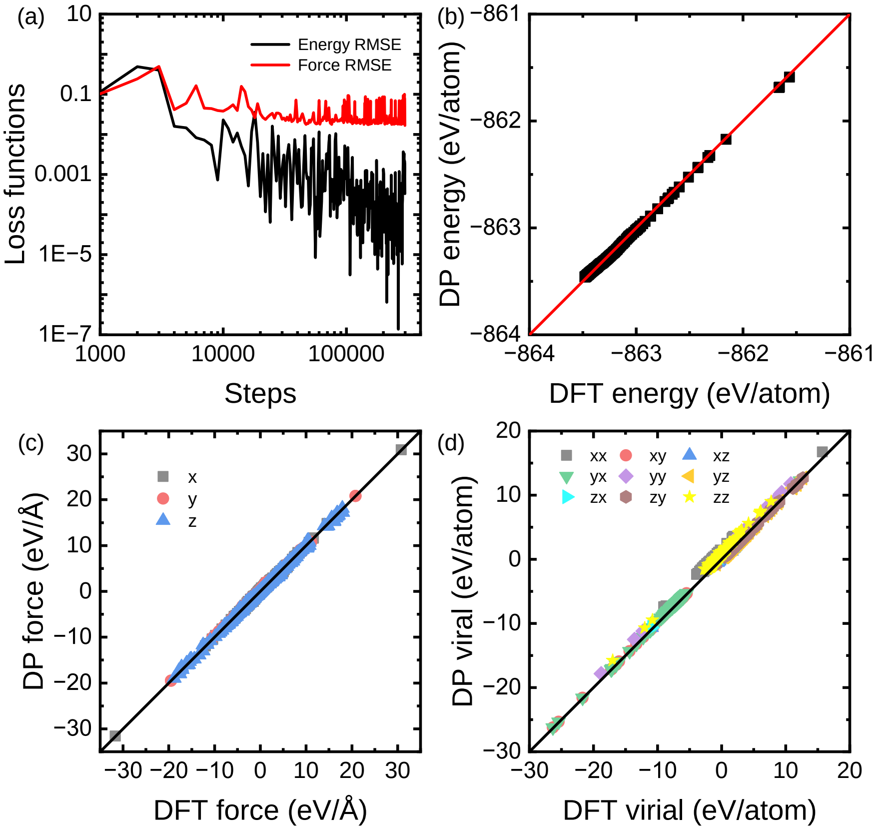

Fig. 2. Training error evolution during the optimization of the DP-MLP model: (a) Energy and force errors as a function of training steps and (b-d) error distributions for energy, force, and virial stress compared with DFT reference.

3. Results and discussion

3.1 Benchmarking of the DP-MLP against DFT

The predictive accuracy and robustness of the developed DP-MLP model are assessed by analyzing the loss function evolution and comparing force error distributions with reference DFT data. Fig. 2(a) presents the convergence behavior of energy and force errors during training. At the initial stage, with randomly initialized parameters, the model exhibits errors of 0.115 eV and 0.103 eV/Å for energy and forces, respectively. Progressive training results in a systematic reduction of quantities, ultimately reaching magnitudes on the order of 10^{-5} eV for energy and 10^{-2} eV/Å for forces. These low errors persist on the validation set, indicating strong generalization capability and stable convergence. The obtained error magnitudes represent a significant improvement over typical empirical potentials, which often fail to simultaneously minimize both energy and force errors. Figs. 2(b)-2(d) further show the error distributions of energy, force, and virial components relative to DFT calculations. The corresponding root-mean-square errors are determined to 0.0186 eV, 0.0382 eV/Å and 0.2230 eV/Å, respectively. These low deviations, achieved at a fraction of the computational cost of full DFT calculations, demonstrate the near-DFT accuracy of DP-MLP. The close agreement between predicted and reference data confirm that DP-MLP maintains numerical stability and reliability across the training domain. Overall, DP-MLP exhibits robust predictive performance for energy, force, and virial quantities, establishing a solid foundation for subsequent MD studies.

3.2 Analysis of radial distribution functions in CO_2 hydrate

Radial distribution functions (RDFs) provide essential insights into the local atomic structure of sI CO_2 hydrate and serve as a critical benchmark for evaluating interatomic potential accuracy. Analysis of the O-H, O-C, and H-C correlations (Fig. 3) demonstrates variations in peak positions, reflecting fundamental differences in how each potential represents interatomic interactions. In the O-H RDF (Fig. 3(a)), the first peak corresponds to the covalent O-H bond within water molecules. DP-MLP model predicts this bond length at approximately 0.963 Å, closely matching the DFT value of around 0.968 Å. This high degree of agreement indicates that DP-MLP reliably captures intramolecular geometry of hydrate framework. The second peak, associated with H-bonding interactions, is located at around 1.76 Å for DP-MLP and empirical models, in good agreement with the DFT result of around 1.78 Å. Medium- and long-range oscillations reflecting cage geometry and lattice periodicity are also captured by DP-MLP, confirming its accuracy in representing the H-bond network and water cage integrity.

For the O-C RDF (Fig. 3(b)), which reflects both in-

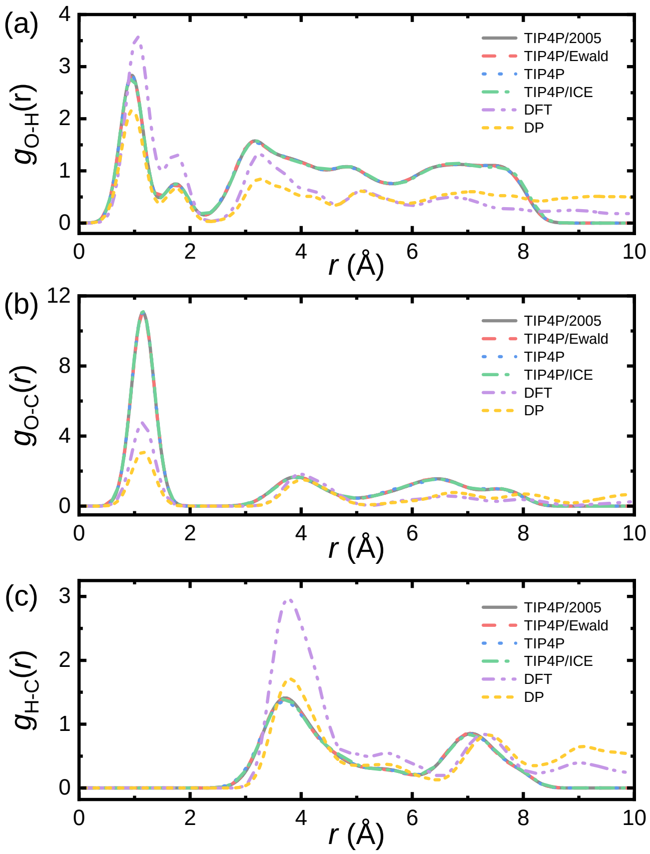

Fig. 3. RDFs of CO_2 hydrate from TIP4P, TIP4P/Ice, TIP4P/2005, and TIP4P/Ewald empirical potentials, DP-MLP, and DFT. (a) O-H RDF, (b) O-C RDF and (c) H-C RDF.

tramolecular C-O bonds in CO_2 and guest-host interactions, DP-MLP continues to show positional accuracy. The first peak, representing the C-O covalent bond, appears at around 1.15 Å, nearly identical to the DFT value of about 1.16 Å. The four empirical models also capture this bond length accurately. The second peak, corresponding to the nearest-neighbor distance between water oxygen and CO_2 carbon, is positioned by DP-MLP at 3.85 Å, matching DFT exactly. This fidelity highlights the capability of DP-MLP to represent guest-host separations that govern vibrational coupling and thermal transport.

The H-C RDF (Fig. 3(c)) provides information on the arrangement of water hydrogens around CO_2 guests, which is essential for understanding local cage packing and guest-host interactions. The principal peak appears at approximately 3.78 Å for both DFT and DP-MLP, while the empirical potentials slightly underestimate this distance (around 3.72 Å). This further demonstrates the superior structural accuracy of DP-MLP. The precise reproduction of key RDF features by DP-MLP, especially the guest-host distances, is crucial as these structural details directly influence the mechanical stability and phonon-mediated thermal transport properties discussed in subsequent sections.

Across all RDFs, DP-MLP consistently reproduces peak positions with high accuracy, capturing bond lengths, guest-host distances, and longer-range cage correlations. In contrast, TIP4P-based empirical models display deviations in peak positions due to their fixed-form forcefields and limited flexibility. DP-MLP therefore provides a robust and transferable representation of interatomic interactions, essential for accurate thermo-mechanical property predictions of CO_2 hydrates in applications such as energy storage, CO_2 sequestration, and natural gas recovery.

3.3 Mechanical responses

The stress-strain responses of crystalline CO_2 hydrate under uniaxial tension as obtained from various potentials are presented in Fig. 4, including empirical potentials (TIP4P/Ewald, TIP4P/Ice, TIP4P, TIP4P/2005) and DP-MLP, as well as DFT as a reference. As indicated, DFT calculations establish the benchmark with the highest ultimate tensile strength of approximately 1.20 GPa. DP-MLP closely reproduces this value with a peak stress of 1.10 GPa. In comparison, empirical TIP4P-type potentials exhibit deviation in their predictions. Among these empirical models, TIP4P/Ice and TIP4P/2005 predict intermediate strengths (around 1.00-1.16 GPa), TIP4P/Ewald yields reduced strength (0.92 GPa), and TIP4P produces the lowest value (0.75 GPa). This clear hierarchy underscores the pronounced forcefield dependence of tensile strength predictions, which DP-MLP mitigates through its close approximation of DFT behavior.

The strain at which peak stress occurs, indicative of failure initiation, also differentiates among potentials. The empirical

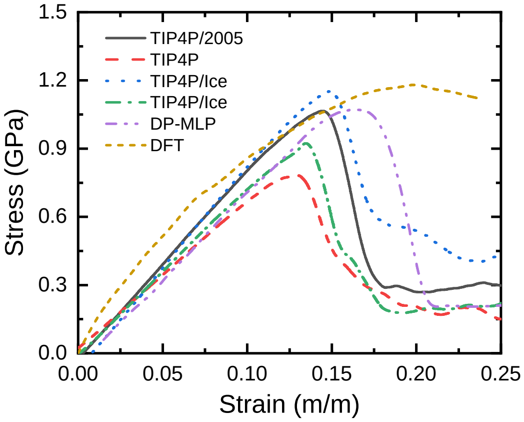

Fig. 4. Stress-strain curve of sI CO_2 hydrate subjected to uniaxial loading predicted by empirical water potentials (TIP4P/Ewald, TIP4P/Ice, TIP4P, TIP4P/2005), DP-MLP potential, and DFT.

water potentials predict failure strains between 0.12-0.15, while DP-MLP yields a slightly delayed peak at 0.16 strain, which remains earlier than the DFT reference peak at 0.19 strain. These discrepancies reflect fundamental differences in how each potential captures the progressive weakening of H-bonded networks and water cage integrity under tensile loading. Beyond the peak stress, post-yield behavior reveals crucial contrasts in perceived material ductility. Both DFT and DP-MLP exhibit a gradual stress delay beyond the maximum stress, accompanied by a sustained load-bearing capacity over a finite strain range, indicating a progressive failure involving continued structural integrity after initial cage rupture. In contrast, the empirical potentials tend to a rapid loss of strength beyond the peak, implying a more brittle type of failure.

The favorable performance of DP-MLP originates from its training on comprehensive DFT datasets including strained and thermally-perturbed states, enabling it to learn both equilibrium bonding and anharmonic deformation pathways. Unlike fixed-form empirical potentials with rigid functional forms and static parameters, DP-MLP adapts to local atomic environments through many-body descriptions, yielding improved accurate modeling of bond stretching, H-bond breaking, and reformation processes. This flexibility allows DP-MLP to better capture energy dissipation mechanisms and structural evolution pathways that govern gradual failure and residual strength retention. The ability to capture post-failure load-bearing behavior is particularly important for predicting CO_2 hydrate stability under external stress perturbations in both natural and engineering settings. Although direct experimental measurements of monocrystalline CO_2 hydrate mechanical properties are not available due to experimental challenges, the predicted tensile strength of 1.10 GPa by DP-MLP falls within the range of values reported for similar clathrate hydrates, providing indirect validation of our mechanical predictions.

3.4 Thermal conductivity

The representative temperature gradient across the hydrate sample used for thermal conductivity evaluation is shown in Fig. 5(a), while Fig. 5(b) compares the thermal conductivities of CO_2 hydrate at 270 K using four empirical potentials of TIP4P, TIP4P/2005, TIP4P/Ewald, and TIP4P/Ice, as well as as-developed DP-MLP, with values of 0.8814±0.05716 W/(m·K), 0.4813±0.05201 W/(m·K), 0.5485±0.01721 W/(m·K), 1.076±0.08404 W/(m·K) and 0.6690±0.04316 W/(m·K), respectively. The reported uncertainties represent the standard deviation from ten independent simulation runs, ensuring statistical significance. To validate the developed DP-MLP model, the thermal conductivity by DP-MLP is compared with experimental measurements. DP-MLP predicts a value of 0.6690±0.04316 W/(m·K), in excellent agreement with the experimental result of around 0.6580 W/(m·K) reported by (Wan et al., 2016), with only 1.67% deviation. This deviation is substantially smaller than those observed with the empirical potentials, which range from approximately -27% to +64%, underscoring the superior accuracy of DP-MLP for predicting thermal transport properties. The quantitative superiority of DP-MLP is evident when comparing the deviation from the experimental value (Wan et al., 2016), with DP-MLP (+1.67%), TIP4P/Ice (+63.5%), TIP4P (+34.0%), TIP4P/Ewald (-16.6%), TIP4P/2005 (-26.9%), respectively. As a result of their fixed mathematical forms with a limited number of parameters and fitting strategies, water empirical potentials exhibit certain limitations in predicting thermal conductivity of CO_2 hydrate, which are unable to fully capture interatomic interactions during atomic motion and bonding (Martinez et al., 2013; Xie et al., 2023; Sun et al., 2025).

3.5 Vibrational dynamics

Thermal transport in clathrate hydrates is predominantly governed by phonon-mediated mechanisms, making the characterization of vibrational properties and atomic dynamics essential for understanding thermal conductivity. The velocity autocorrelation function (VACF) and phonon density of states (PDOS) provide critical insights into the phonon behavior and energy distribution within the crystal lattice (Dickey and Paskin et al., 1969). These analyses allow evaluation of the accuracy of various potential models to capture the fundamental vibrational characteristics that influence heat transfer. Here, the VACF ($C(t)$) is calculated as follows:

$$C(t)=\frac{1}{N}\sum_{i=1}^{N}\langle v_i(0)v_i(t)\rangle \tag{2}$$

where $V_i(t)$ and N are the velocity vector of particle i at time t and the total number of atoms in the hydrate system. The ensemble average <> is obtained by sampling velocities at regular intervals during the simulation period and averaging over time origins. The PDOS ($g(\omega)$) is derived from the Fourier transform of the VACF:

$$g(\omega)=\int_{-\infty}^{\infty}e^{i\omega t}C(t)dt \tag{3}$$

where ω is the vibration frequency. Here, the simulations span a period of 2.5 ps, with atomic velocities sampled every 0.5 fs. As the VACF is normalized, the PDOS is expressed in units of THz^{-1}.

The VACF and PDOS profiles of CO_2 hydrate obtained

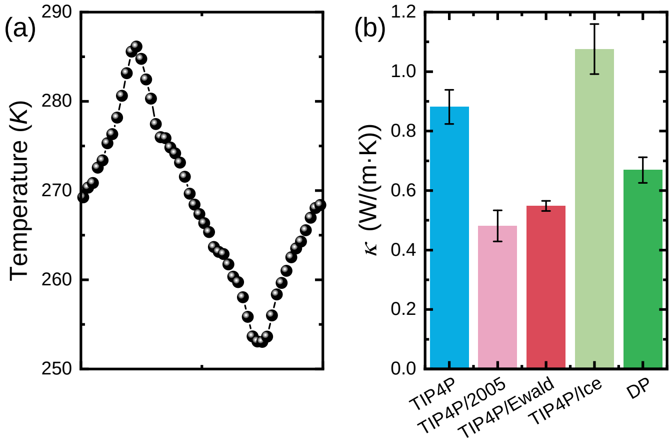

Fig. 5. Thermal conductivity of sI CO_2 hydrate using different potential models: (a) Representative temperature gradient profile across the hydrate sample and (b) comparison of thermal conductivity values from empirical potentials and the DP-MLP model.

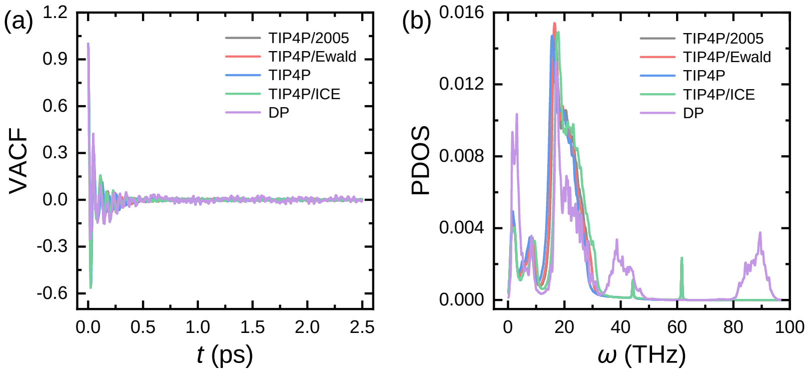

Fig. 6. (a) VACF and (b) PDOS of CO_2 hydrate computed with TIP4P, TIP4P/2005, TIP4P/Ewald, and TIP4P/Ice empirical potentials and DP-MLP model.

from the four empirical potentials and the DP-MLP model are compared in Fig. 6. As shown in Fig. 6(a), the VACF curves, which indicate dynamical stability, exhibit comparable oscillatory behavior and decay rates across all models, converging to zero after approximately 0.5 ps, indicating the system stability. In contrast, notable discrepancies appear in the PDOS spectra (Fig. 6(b)). DP-MLP model yields a higher first peak below 10 THz and reduced intensity near 17 THz compared to empirical potentials. While low-frequency regions (< 30 THz) remain consistent across models, DP-MLP spectrum shows broader and upshifted peaks at higher frequencies, indicating phonon mode hardening and more accurate representation of high-frequency vibrational modes. These differences in PDOS, particularly the enhanced high-frequency content in DP-MLP, are consistent with its more anharmonic potential energy surface and relate directly to variations in predicted thermal conductivity and mechanical failure behavior, as these vibrational modes contribute to energy dissipation and scattering.

To elucidate element-specific dynamics, Fig. 7 presents the VACF and PDOS curves decomposed into atomic contributions (C, H and O). The DP-MLP model consistently yields lower VACF amplitudes (Figs. 7(a)-7(e)), suggesting more damped atomic motion. The comparison of PDOS curves (Figs. 7(d)-7(f)) reveal similar profiles for O- and C-atoms across models, consistent with the dominant role of H-bonded network in thermal transport. However, the H-PDOS (Fig. 7(e)) under DP-MLP model displays enhanced high-frequency contributions despite agreement with empirical potentials at lower frequencies. This indicates that DP-MLP more comprehensively captures high-frequency vibrational behavior, improving the representation of atomic dynamics across the entire spectral range.

3.6 Analysis of phonon localization via phonon participation rate

To gain deeper insight into phonon behavior and quantitatively assess phonon localization, which is key to understanding thermal transport mechanisms in CO_2 hydrate, the phonon participation rate (PPR) is evaluated (Liang et al., 2020; Zhou et al., 2020; Xu et al., 2022). The PPR helps distinguish between extended and localized vibrational modes, providing essential information about phonons contributions to heat conduction. Without requiring full lattice dynamics calculation, the PPR at a given temperature can be directly obtained from MD simulations using (Bell and Dean et al., 1970; Liang et

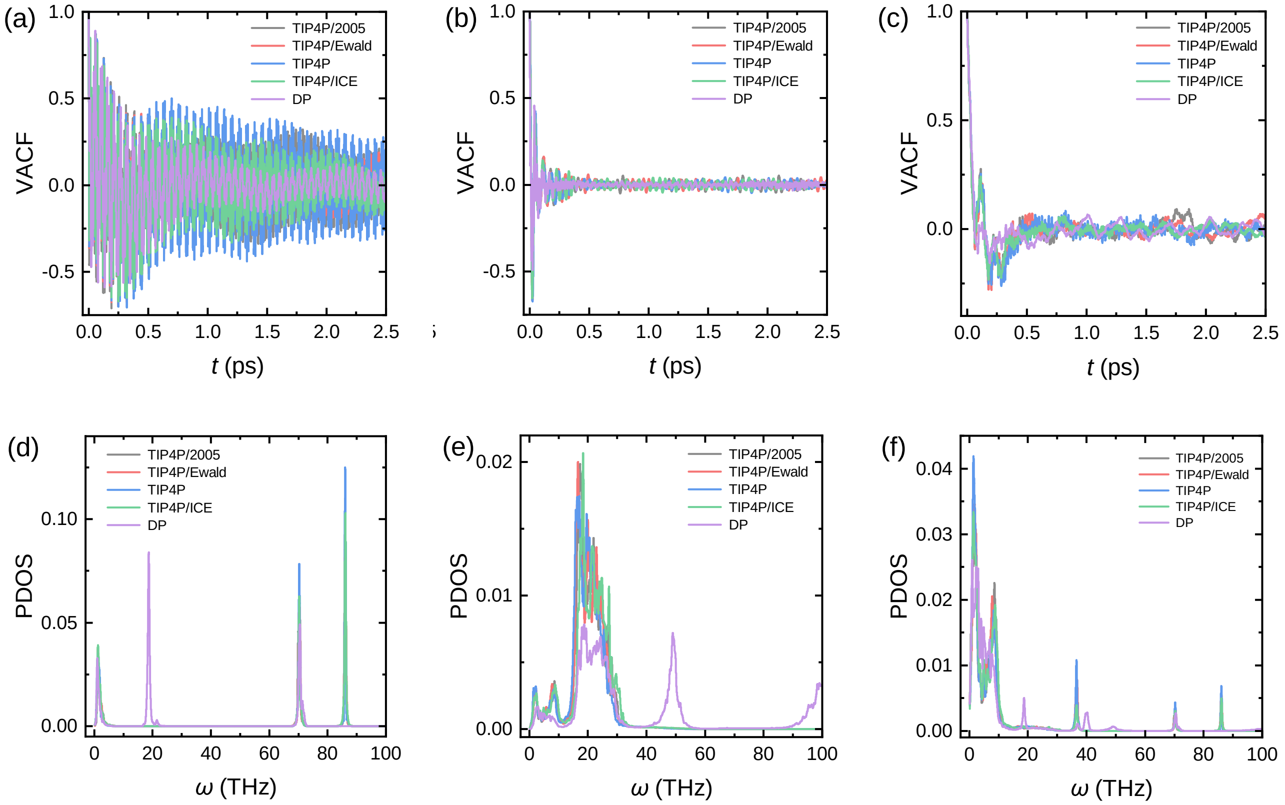

Fig. 7. Element-resolved vibrational properties of CO_2 hydrate: (a-c) VACF curves for C, H, and O atoms under TIP4P, TIP4P/2005, TIP4P/Ewald, and TIP4P/Ice empirical potentials and DP-MLP model and (d-f) PDOS spectra for C, H, and O atoms under TIP4P, TIP4P/2005, TIP4P/Ewald, and TIP4P/Ice empirical potentials and DP-MLP model.

al., 2020; Li et al., 2025):

$$P(\omega) = \frac{1}{N}\frac{\left(\sum_i g_i(\omega)^2\right)^2}{\sum_i g_i(\omega)^4} \tag{4}$$

where $P(\omega)$ represents the PPR at frequency ω , and $g_i(\omega)$ denotes the PDOS of atoms i at frequency ω. The PPR is computed for C-, H-, and O-atoms using both empirical potentials and the DP-MLP model. As shown in Fig. 8(a), the C-atomic PPR values obtained by DP-MLP exceeds that of empirical potentials below 30 THz, but falls below them at higher frequencies. This implies that empirical potentials describe C-phonon modes as more delocalized, while the DP-MLP model indicates stronger delocalization at lower frequencies. Given that C-atoms originate from guest CO_2 molecules, these differences highlight variations in the treatment of guest-host and guest-guest interactions between empirical potentials and DP-MLP.

For H-atoms (Fig. 8(b)), DP-MLP exhibits more extended phonon characteristics in the 0-10 THz and 35-100 THz ranges, but higher localization within 10-35 THz. For O-atoms (Fig. 8(c)), DP-MLP model shows stronger delocalization at high frequencies (55-100 THz). Since H- and O-atoms constitute the hydrate framework, these results indicate that DP-MLP captures more extended phonon modes at both low- (0-10 THz) and high frequencies, while empirical potentials yield greater delocalization within 10-35 THz.

These discrepancies arise because empirical potentials rely on fixed potential forms parameterized for specific interactions (Martinez et al., 2013; Xie et al., 2023; Sun et al., 2025), while DP-MLP is trained on datasets derived from the DFT datasets, whose size and quality directly impact the accuracy of high-frequency vibrational modes. The PPR results thus reflect pronounced differences in atomic dynamics, with DP-MLP offering a more detailed account of high-frequency phonon behavior. The distinct PPR profiles underscore different physical pictures. DP-MLP suggests strongly coupled guest-host dynamics at low frequencies and framework-dominated extended modes at very high frequencies, with implications for frequency-dependent phonon scattering rates and thermal conductivity.

3.7 Spectral energy density and phonon dispersion

To further elucidate lattice dynamics and phonon transport properties of CO_2 hydrate, the spectral energy density (SED) is computed (Li et al., 2023; Ying et al., 2023; Zeng et al., 2024). The SED provides a spatial and frequency-resolved representation of vibrational energy distribution, offering valuable insights into phonon dispersion and scattering behavior. The SED Φ is a function of wave vector and frequency , and is calculated as (Thomas et al., 2010; Liang et al., 2025):

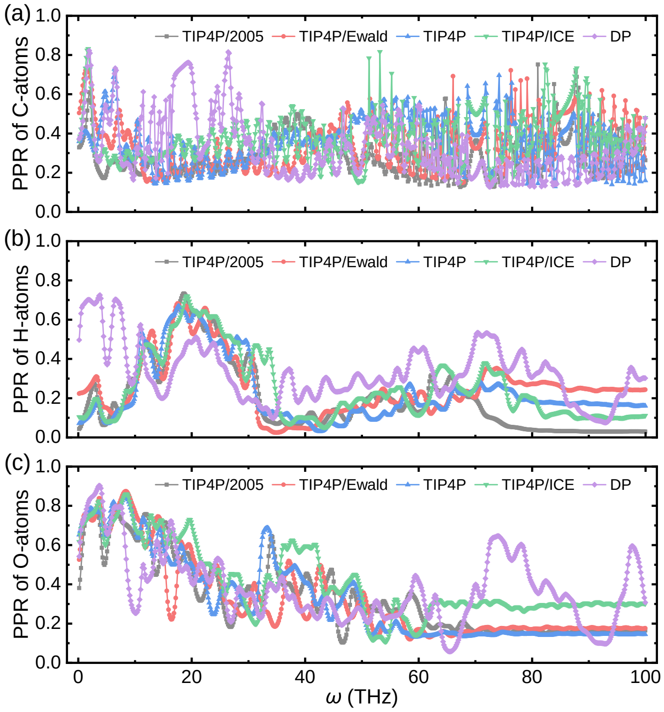

Fig. 8. Atomic phonon participation rate (PPR) for CO_2 hydrate. (a) C-PPR, (b) H-PPR and (c) O-PPR.

$$\Phi(\vec{k},\omega)=\frac{1}{4\pi\tau_0 N}\sum_{\alpha,b} m_b \left\|\int_0^{t_0}\sum_N v_\alpha(N,b)\times \exp\left[i\vec{k}\cdot\vec{r}(N,0)-i\alpha t\right]dt\right\|^2 \tag{5}$$

where t_0, m_b and v_a are the integration time, the mass of atom b, and the atomic velocity along the a direction in the N cell. In addition, $\vec{r}$ represents the equilibrium position vector of the atom, and i denotes the imaginary number.

The SED of CO_2 hydrate computed using empirical potentials and DP-MLP is presented in Fig. 9. It is observed that in the low-frequency range of 0-1 THz, both empirical potentials and DP-MLP exhibit clear and comparable numbers of acoustic branches, indicating similar predictions of hydrate stability. At higher frequencies, optical branches overlap significantly due to the complex atomic structure of the hydrate system. While phonon spectra show considerable similarity despite differences in interatomic potential formulations between empirical potentials and DP-MLP.

As shown in Fig. 9, the acoustic branches in the SED spectrum derived from DP-MLP exhibit broader and more diffuse profiles compared to the distinct linear features in empirical potentials. Quantitatively, DP-MLP results show a full-width-at-half-maximum for the acoustic branches that is approximately twice that observed in empirical potentials, indicating significantly stronger phonon scattering. Given that clathrate hydrates are inherently disordered, dynamic systems with strong anharmonicity (Schober et al., 2003; Tse et al., 2005; Udachin et al., 2007; Arora et al., 2016), the enhanced broadening and nonlinearity in DP-MLP results reflect more pronounced phonon scattering at low-frequencies. This suggests that DP-MLP model more effectively captures strong scattering effects and complex interatomic interactions characteristic of hydrate system. In contrast, empirical potentials, due to their inherent limitations in representing H-bond rigidity and atomic disorder, tend to underestimate atomic disorder and anharmonicity effects, leading to less pronounced scattering features in SED spectra.

3.8 Phonon lifetime

To further understand the phonon scattering behavior and thermal transport properties, phonon lifetimes are calculated. Phonon lifetime serves as a critical indicator of phonon scattering intensity and provides direct insight into the thermal resistance mechanisms. The lifetime corresponding to a specific phonon mode is obtained by fitting the SED peak with a Lorentzian function (Zhou et al., 2020):

$$\Phi(\vec{k},\omega)=\frac{I}{1+[(\omega-\omega_c)/g]^2} \tag{6}$$

where I represents the peak amplitude of the SED and ω_c is the frequency of the peak center. g denotes the half width of the half-peak. The phonon lifetime at frequency ω is then given by $t = 0.5g$.

The phonon lifetimes in CO_2 hydrate obtained from empirical potentials and DP-MLP are shown in Fig. 10. Phonon lifetimes computed using DP-MLP are systematically shorter than those obtained from empirical potentials, particularly in the low-frequency range of 0-1 THZ. This frequency region is critical as acoustic phonon branches dominate the thermal transport properties of the hydrate system. The reduced lifetimes indicate stronger phonon scattering in DP-

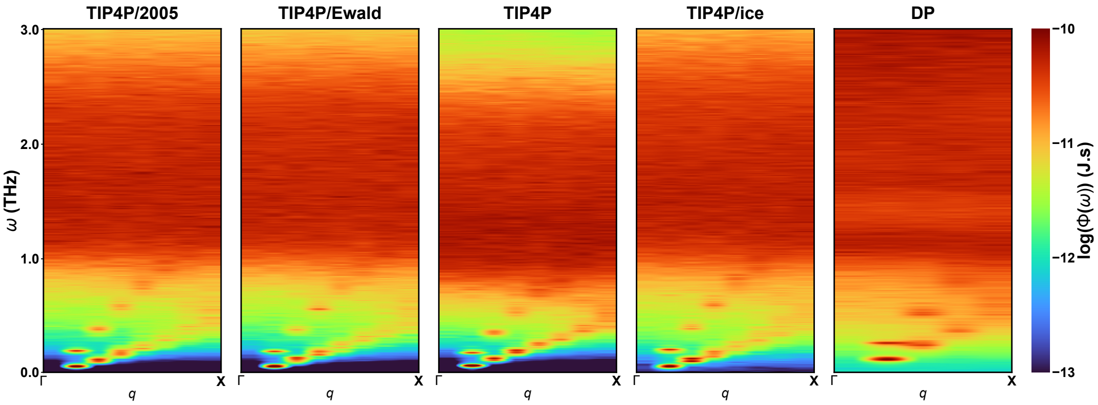

Fig. 9. Spectral energy density (SED) of CO_2 hydrate computed using different potential models. (a) TIP4P/2005, (b) TIP4P/Ewald, (c) TIP4P and (d) TIP4P/Ice and (e) DP-MLP. DP-MLP model (e) shows notably broader and less distinct acoustic branches below 2 THz, signifying enhanced phonon scattering compared to the sharper branches in empirical potentials.

MLP, consistent with broader SED profiles observed in Fig. 9. The reduced lifetimes calculated from DP-MLP can be attributed to its more comprehensive description of disorder-induced and anharmonic scattering mechanisms. By more accurately capturing the complex interatomic interactions, DP-MLP reveals enhanced phonon scattering that impedes heat transfer, leading to the observed reduction in phonon lifetimes. In contrast, empirical potentials, with similar functional forms, tend to underestimate these scattering effects. The consistently shorter phonon lifetimes predicted by DP-MLP, especially for heat-carrying low-frequency acoustic phonons, provide a direct microscopic explanation for its prediction of lower thermal conductivity that agrees well with experiments, contrasting with overestimation by empirical potentials.

Therefore, the DP-MLP potential offer several distinct advantages. First, it preserves phonon thermal transport properties and atomic dynamic behavior consistent with empirical potentials in thermal conductivity calculations. Second, it captures atomic vibrations over an extended frequency range, including high-frequency modes, while maintaining improved stability. Most importantly, it more faithfully represents strong scattering effects resulting from atomic disorder and system anharmonicity, thereby offering a more physically realistic representation of complex intermolecular interactions in CO_2 hydrate.

3.9 Correlating mechanical, thermal, and vibrational properties

The integrated analysis of mechanical response, thermal transport, and vibrational dynamics reveals consistent picture of superior physical fidelity of DP-MLP. The accurate prediction of progressive ductile-like failure under tension by DP-MLP is intrinsically linked to its realistic portrayal of H-bond network anharmonicity, evidenced by broader SED profiles and enhanced high-frequency contributions in the H-PDOS. This anharmonicity facilitates energy dissipation through phonon scattering mechanisms that also governs thermal conductivity. The shorter phonon lifetimes and broader SED peaks predicted by DP-MLP directly correlate with its prediction of lower, more accurate thermal conductivity compared to most empirical potentials. Furthermore, element-specific phonon participation rates indicate that DP-MLP captures stronger coupling between guest molecules and host water cage, influencing both mechanical stability and phonon scattering processes. These interconnected findings demonstrate that DP-MLP not only improve individual property predictions but provides a coherent, multi-faceted description of CO_2 hydrate systems where mechanical and thermal properties emerge from unified representation of underlying interatomic interactions.

4. Conclusions

In summary, a DP-MLP was developed and validated specifically for CO_2 hydrate. The DP-MLP model demonstrate good fidelity in reproducing DFT benchmarks for energies, forces, virial stresses, and RDFs. When applied in large-scale MD simulation, DP-MLP revealed stress-strain behavior consistent with DFT predictions, including elastic strain range, tensile strength, and ductile-like post-failure response. In addition, NEMD simulations produced thermal conductivity values in near-quantitative agreement with experimental measurements, demonstrating reliability of DP-MLP model for heat transport studies. Analyses of vibrational dynamics, PDOSs, and SED confirmed that DP-MLP more realistically represents anharmonic effects, phonon scattering, and high-frequency vibrational modes compared with empirical potentials. These results establish DP-MLP as a robust and efficient surrogate for first-principles methods, enabling accurate and scalable exploration of CO_2 hydrate mechanics and thermal transport. The integrated analysis demonstrates that DP-MLP provides a physically consistent descriptions across mechanical, thermal, and vibrational properties, capturing intrinsic coupling between these phenomena in hydrate systems. This framework provides a powerful computational foundation for advancing hydrate-based CCS and refrigeration technologies. The accuracy and efficiency of DP-MLP open avenues for future studies on more complex and realistic hydrate systems, including those with defects, impurities, or under non-

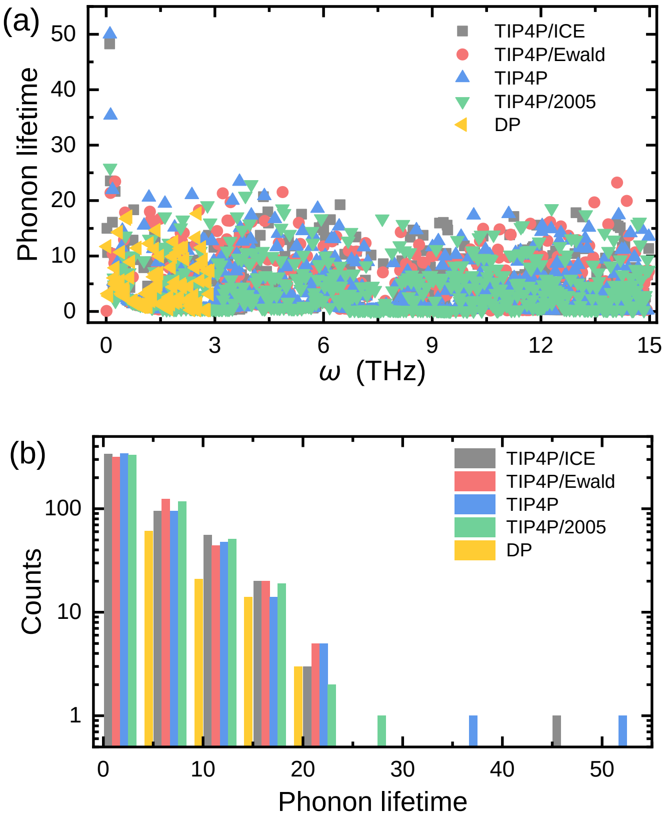

Fig. 10. Phonon lifetimes in CO_2 hydrate. (a) Phonon lifetime as a function of frequency and (b) distribution profiles of phonon lifetime under TIP4P, TIP4P/2005, TIP4P/Ewald, and TIP4P/Ice empirical potentials, and DP-MLP model.

equilibrium conditions.

Acknowledgements

This work is financially supported by the National Natural Science Foundation of China (Nos. 12172314 and 12572127), and the 111 project (No. B16029). The supercomputer GPU hours are provided by Shaorong Fang and Tianfu Wu from Information and Network Center of Xiamen University are acknowledged for the help with the high-performance computer.

References

Abascal, J. L. F., Sanz, E., García Fernández, R., et al. A potential model for the study of ices and amorphous water: TIP4P/Ice. The Journal of Chemical Physics, 2005, 122(23): 234511.

Abascal, J. L. F., Vega, C. A general purpose model for the condensed phases of water: TIP4P/2005. The Journal of Chemical Physics, 2005, 123(23): 234505.

Arora, R., Basu, A., Mianjy, P., et al. Understanding deep neural networks with rectified linear units. Paper presented at International Conference on Learning Representations, 2018, Vancouver, Canada.

Bell, R. J., Dean, P. Atomic vibrations in vitreous silica. Discussions of the Faraday Society, 1970, 50: 55-61.

Berendsen, H. J. C., Grigera, J. R., Straatsma, T. P. The missing term in effective pair potentials. The Journal of Physical Chemistry, 1987, 91(24): 6269-6271.

Chen, L., Sun, C., Chen, G., et al. Measurements of hydrate equilibrium conditions for CH_4, CO_2, and $CH_4 + C_2H_6 + C_3H_8$ in various systems by step-heating method. Chinese Journal of Chemical Engineering, 2009, 17(4): 635-641.

Dickey, J. M., Paskin, A. Computer simulation of the lattice dynamics of solids. Physical Review, 1969, 188(3): 1407-1418.

Hafner, J. Ab-initio simulations of materials using vasp: Density-functional theory and beyond. Journal of Computational Chemistry, 2008, 29(13): 2044-2078.

Hagler, A. T., Lifson, S., Dauber, P. Consistent force field studies of intermolecular forces in hydrogen-bonded crystals. 2. A benchmark for the objective comparison of alternative force fields. Journal of the American Chemical Society, 1979, 101(18): 5122-5130.

Harris, J. G., Yung, K. H. Carbon dioxide's liquid-vapor coexistence curve and critical properties as predicted by a simple molecular model. The Journal of Physical Chemistry, 1995, 99(31): 12021-12024.

Hassanpouryouzband, A., Joonaki, E., Vasheghani Farahani, M., et al. Gas hydrates in sustainable chemistry. Chemical Society Reviews, 2020, 49(15): 5225-5309.

Horn, H. W., Swope, W. C., Pitera, J. W., et al. Development of an improved four-site water model for biomolecular simulations: TIP4P-Ew. The Journal of Chemical Physics, 2004, 120(20): 9665-9678.

Jia, J., Liang, Y., Tsuji, T., et al. Elasticity and stability of clathrate hydrate: Role of guest molecule motions. Scientific Reports, 2017, 7(1): 1290.

Jiang, H., Jordan, K. D. Comparison of the properties of xenon, methane, and carbon dioxide hydrates from equilibrium and nonequilibrium molecular dynamics simulations. The Journal of Physical Chemistry C, 2010, 114(12): 5555-5564.

Jiao, L.-J., Wan, R.-C., Wang, Z.-L. Experimental investigation of CO_2 hydrate dissociation in silica nanoparticle system with different thermal conductivity. International Journal of Thermophysics, 2021, 42(12): 170.

Jorgensen, W. L., Chandrasekhar, J., Madura, J. D., et al. Comparison of simple potential functions for simulating liquid water. The Journal of Chemical Physics, 1983, 79(2): 926-935.

Jorgensen, W. L., Maxwell, D. S., Tirado-Rives, J. Development and testing of the OPLS all-atom force field on conformational energetics and properties of organic liquids. Journal of the American Chemical Society, 1996, 118(45): 11225-11236.

Kang, S. P., Lee, H., Lee, C. S., et al. Hydrate phase equilibria of the guest mixtures containing CO_2, N_2 and tetrahydrofuran. Fluid Phase Equilibria, 2001, 185(1): 101-109.

Kresse, G., Furthmüller, J. Efficiency of ab-initio total energy calculations for metals and semiconductors using a plane-wave basis set. Computational Materials Science, 1996, 6(1): 15-50.

Li, J., Ying, P., Liang, T., et al. Mechanical and thermal properties of graphyne-coated carbon nanotubes: A molecular dynamics simulation on one-dimensional all-carbon van der waals heterostructures. Physical Chemistry Chemical Physics, 2023, 25(12): 8651-8663.

Li, Y., Xiong, K., Qu, Y., et al. Effects of guest molecular occupancy and electric field on thermal conductivity of CO_2 hydrates. The Journal of Chemical Physics, 2025, 163(8): 084504.

Liang, T., Jiang, W., Xu, K., et al. Pysed: A tool for extracting kinetic-energy-weighted phonon dispersion and lifetime from molecular dynamics simulations. Journal of Applied Physics, 2025, 138(7): 075101.

Liang, T., Zhou, M., Zhang, P., et al. Multilayer in-plane graphene/hexagonal boron nitride heterostructures: Insights into the interfacial thermal transport properties. International Journal of Heat and Mass Transfer, 2020, 151: 119395.

Lin, Y., Liu, Y., Xu, K., Li, T., Zhang, Z., Wu, J. Strengthening and weakening of methane hydrate by water vacancies. Advances in Geo-Energy Research, 2022, 6(1): 23-37.

Liu, J. J., Fu, R., Lin, Y. W., et al. Mechanical destabilization and cage transformations in water vacancy-contained CO_2 hydrates. ACS Sustainable Chemistry & Engineering, 2022, 10(31): 10339-10350.

Liu, N., Hong, C., Liu, X. Effects of nanoparticles on CO_2 hydrate thermal conductivity. CIESC Journal, 2017, 68(9): 5.

Liu, T.-S., Liu, N., Hong, C.-F. Molecular dynamics simulation of thermal conductivity of CO_2 hydrate. Journal of Atomic and Molecular Physics, 2021, 38(4): 6.

Lu, C., Qin, X., Sun, J., Wang, R., Cai, J. Research progress and scientific challenges in the depressurization exploitation mechanism of clayey-silt natural gas hydrates in the northern South China Sea. Advances in Geo-Energy Research, 2023, 10(1): 14-20.

Luo, K., Shen, Y., Li, J., et al. Pressure-induced stability of methane hydrate from machine learning force field simulations. The Journal of Physical Chemistry C, 2023, 127(15): 7071-7077.

Martinez, J. A., Yilmaz, D. E., Liang, T., et al. Fitting empirical potentials: Challenges and methodologies. Current Opinion in Solid State and Materials Science, 2013, 17(6): 263-270.

Plimpton, S. Fast parallel algorithms for short-range molecular dynamics. Journal of Computational Physics, 1995, 117(1): 1-19.

Potoff, J. J., Siepmann, J. I. Vapor-liquid equilibria of mixtures containing alkanes, carbon dioxide, and nitrogen. AIChE Journal, 2001, 47(7): 1676-1682.

Schober, H., Itoh, H., Klapproth, A., et al. Guest-host coupling and anharmonicity in clathrate hydrates. The European Physical Journal E, 2003, 12(1): 41-49.

Shi, Q., Cao, P., Han, Z., et al. Role of guest molecules in the mechanical properties of clathrate hydrates. Crystal Growth & Design, 2018, 18(11): 6729-6741.

Song, Z., Li, Y., Shi, Q., et al. Diffusion, mechanical and thermal properties of sT hydrogen hydrate by machine learning potential. Journal of Physics: Condensed Matter, 2025, 37(11): 115102.

Sun, Z., Wang, Y., Li, W., et al. A high accuracy machine-learning potential model for Mo-Re binary alloy. Computational Materials Science, 2025, 254: 113870.

Takeuchi, F., Hiratsuka, M., Ohmura, R., et al. Water proton configurations in structures I, II, and H clathrate hydrate unit cells. The Journal of Chemical Physics, 2013, 138(12): 124504.

Targ, S., Almeida, D., Lyman, K. Resnet in resnet: Generalizing residual architectures. arXiv preprint arXiv:1603.08029, 2016.

Thomas, J. A., Turney, J. E., Iutzi, R. M., et al. Predicting phonon dispersion relations and lifetimes from the spectral energy density. Physical Review B, 2010, 81(8): 081411.

Tse, J. S., Klug, D. D., Zhao, J. Y., et al. Anharmonic motions of Kr in the clathrate hydrate. Nature Materials, 2005, 4(12): 917-921.

Udachin, K. A., Ratcliffe, C. I., Ripmeester, J. A. Structure, Dynamics and Ordering in Structure I Ether Clathrate Hydrates from Single-Crystal X-ray Diffraction and ^{2}H NMR Spectroscopy. The Journal of Physical Chemistry B, 2007, 111(39): 11366-11372.

Wan, L., Liang, D., Li, D., et al. Characteristics of thermal conductivity and thermal diffusivity of carbon dioxide hydrate. CIESC Journal, 2016, 67(10): 7.

Wan, L. H., Liang, D. Q., Guan, J. A. Molecular dynamics study of thermal conduction in carbon dioxide hydrates. Advanced Materials Research, 2014, 1008-1009: 861-

872.

Wang, H., Zhang, L. F., Han, J. Q., et al. Deepmd-kit: A deep learning package for many-body potential energy representation and molecular dynamics. Computer Physics Communications, 2018, 228: 178-184.

Warrier, P., Naveed Khan, M., Carreon, M. A., et al. Integrated gas hydrate-membrane system for natural gas purification. Journal of Renewable and Sustainable Energy, 2018, 10(3): 034701.

Xia, Y., Elsworth, D., Xu, S., et al. Pore-scale gas–water two-phase flow and relative permeability characteristics of disassociated hydrate reservoir. Petroleum Science, 2025, 22(8): 3344-3356.

Xie, S. R., Rupp, M., Hennig, R. G. Ultra-fast interpretable machine-learning potentials. npj Computational Materials, 2023, 9(1): 162.

Xu, K., Hao, Y., Liang, T., et al. Accurate prediction of heat conductivity of water by a neuroevolution potential. The Journal of Chemical Physics, 2023, 158(20): 204114.

Xu, K., Liang, T., Zhang, Z., et al. Grain boundary and misorientation angle-dependent thermal transport in single-layer MoS_2. Nanoscale, 2022, 14(4): 1241-1249.

Xu, K., Yang, L., Liu, J., et al. Mechanical properties of CH_4-CO_2 heteroclathrate hydrates. Energy & Fuels, 2020, 34(11): 14368-14378.

Yin, Z., Zheng, J., Kim, H., et al. Hydrates for cold energy storage and transport: A review. Advances in Applied Energy, 2021, 2: 100022.

Ying, P. H., Liang, T., Xu, K., et al. Sub-micrometer phonon mean free paths in metal-organic frameworks revealed by machine learning molecular dynamics simulations. ACS Applied Materials & Interfaces, 2023, 15(30): 36412-36422.

Zeng, J., Liang, T., Zhang, J., et al. Correlating young's modulus with high thermal conductivity in organic conjugated small molecules. Small, 2024, 20(21): 2309338.

Zhang, F., Ni, H., Wang, Y., et al. Molecular dynamics study on mechanical properties of CO_2-N_2 heteroclathrate hydrates. Crystal Growth & Design, 2023, 23(4): 2239-2247.

Zhang, J., Fu, H. -Q., Guo, M. -Z., et al. New insights into the deposition of natural gas hydrate on pipeline surfaces: A molecular dynamics simulation study. Petroleum Science, 2024a, 21(1): 694-704.

Zhang, Y., Liu, X. T., Shi, Q., et al. Mechanical properties and cage transformations in CO_2-CH_4 heterohydrates: A molecular dynamics and machine learning study. Journal of Physics D-Applied Physics, 2024b, 57(46): 465302.

Zhang, Y., Song, Z. X., Lin, Y. W., et al. Predicting mechanical properties of CO_2 hydrates: Machine learning insights from molecular dynamics simulations. Journal of Physics-Condensed Matter, 2024c, 36(1): 015101.

Zhang, Y., Wang, H., Chen, W., et al. Dp-gen: A concurrent learning platform for the generation of reliable deep learning based potential energy models. Computer Physics Communications, 2020, 253: 107206.

Zhang, Z., Duan, Z. An optimized molecular potential for carbon dioxide. The Journal of Chemical Physics, 2005, 122(21): 214507.

Zhou, M., Liang, T., Wu, B., et al. Phonon transport in antisite-substituted hexagonal boron nitride nanosheets: A molecular dynamics study. Journal of Applied Physics, 2020, 128(23): 234304.